
Multi-fidelity Emulator for Cosmological Large Scale 21 cm Lightcone Images: a Few-shot Transfer Learning Approach with GAN

Kangning Diao¹ Yi Mao¹

Abstract

Large-scale numerical simulations ($\gtrsim 500\text{Mpc}$) of cosmic reionization are required to match the large survey volume of the upcoming Square Kilometre Array (SKA). We present a multi-fidelity emulation technique for generating large-scale lightcone images of cosmic reionization. We first train generative adversarial networks (GAN) on small-scale simulations and transfer that knowledge to large-scale simulations with hundreds of training images. Our method achieves high accuracy in generating lightcone images, as measured by various statistics with mostly percentage errors. This approach saves computational resources by 90% compared to conventional training methods. Our technique enables efficient and accurate emulation of large-scale images of the Universe.

1. Introduction

In preparation for the upcoming era of 21 cm cosmology, many models have been developed to extract information from observations. These models range from the semi-numerical simulation, e.g. 21CMFAST (Mesinger et al., 2011; Murray et al., 2020) to hydrodynamical radiation transfer simulation, e.g. THESAN (Kannan et al., 2021), with varying levels of accuracy and computational cost. In addition, different approaches have been applied to infer cosmological and astrophysical parameters, including the Markov Chain Monte Carlo (MCMC) code, e.g. 21CMCMC (Greig & Mesinger, 2017) to the machine learning boosted simulation-based inference (e.g. Alsing et al., 2019; Zhao et al., 2022). However, parameter inference typically requires many forward simulations. Given the large field of view of the next-generation telescopes, large-scale simulations are required to fully exploit the information contained

in the observations. However, these large-scale simulations are computationally expensive, which has inspired the development of emulators as an alternative.

Building emulators typically requires numerous training samples. For large-scale simulations, the cost of obtaining these training samples can be prohibitive in and of itself. To address this issue, the concept of multi-fidelity emulation (Kennedy & O’Hagan, 2000; Ho et al., 2021) has been proposed. This approach first uses low-cost (low-fidelity) simulations to create an emulator. The emulator is then calibrated with a small number of high-cost (high-fidelity) simulations, reducing the computational cost while still maintaining the output quality.

Here we choose GAN (Goodfellow et al., 2014; List & Lewis, 2020; Andrianomena et al., 2022) as our emulation model. GAN emulation has previously demonstrated the ability to produce high-quality samples. However, GAN training is known to suffer very often from mode collapse, especially with a dataset smaller than ~ 1000 images. In the context of 21 cm lightcone emulation, this would typically require $\gtrsim 1000$ expensive simulations which are sometimes impossibly costly. In this paper, we propose the few-shot transfer learning (e.g. Ojha et al., 2021) to train a faithful large-scale 21 cm lightcone image emulator with a limited number of simulations. Few-shot transfer learning allows us to learn a new task with a limited number of samples, which serves as the ‘calibrating’ procedure in multi-fidelity emulation. This multi-fidelity emulation allows us to significantly reduce the number of simulations required to train an accurate lightcone image emulator.

2. Methodology

Our approach involves a two-step process. First, we train our GAN with 120000 small-scale (size of $(2, 64, 512)$) images. In the second step, we train our large-scale GAN on 320 large-scale (size of $(2, 256, 512)$) images while preserving the diversity of GAN results. We will explain our approach in detail in the following.

StyleGAN 2: The GAN architecture used in this work is StyleGAN 2 (Karras et al., 2020). Our generator G consists of two parts: First, a mapping network f takes the astro-

¹Department of Astronomy, Tsinghua University, Beijing, China. Correspondence to: Kangning Diao <dkn16@foxmail.com>, Yi Mao <ymao@tsinghua.edu.cn>.

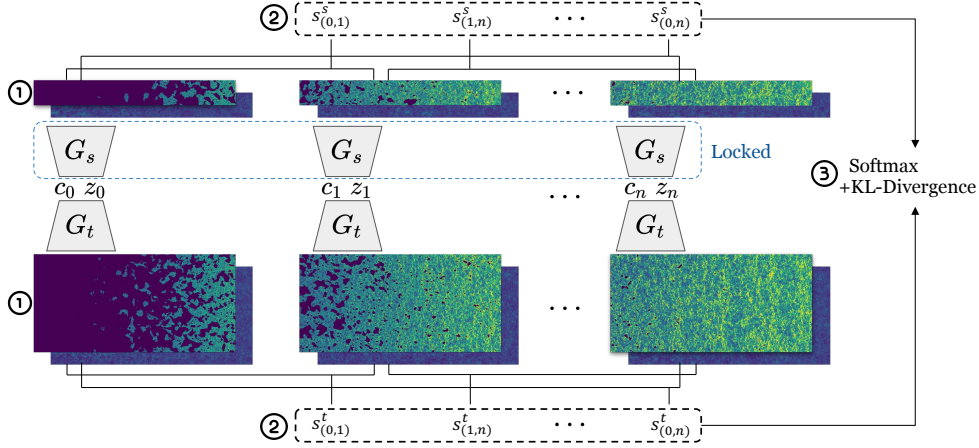


Figure 1. An illustration of the cross-domain correspondence (CDC). ① We first generate a set of samples with both small-scale GAN and large-scale GAN. ② We then calculate the similarity between each image pair generated by the same GAN. ③ Finally, we normalize the similarity vector of each GAN with softmax, then compute the KL-divergence as the CDC. The samples shown here are results from our large-scale GAN.

physical parameter \mathbf{c} and a random vector \mathbf{z} and returns a style vector \mathbf{w} . Second, a synthesis network g uses the style vector \mathbf{w} to shift the weights in convolution kernels, and Gaussian random noise is injected into the feature map right after each convolution to provide variations in different scales of features. Our discriminator D has a ResNet (He et al., 2015)-like architecture.

Cross-Domain Correspondence (CDC): Assuming we have a good small-scale StyleGAN emulator, we expand the size of the generator’s first layer, resulting in a final output size of $(2, 256, 512)$.

Next, we retrain our GAN with large-scale images. We first employ the patchy-level discriminator and cross-domain correspondence as described in Ojha et al. (2021). We mark the small-scale GAN as our source model G_s and the large-scale GAN as the target model G_t . First, we use the same batch of vectors (\mathbf{z}, \mathbf{c}) feeding both G_s and G_t , getting the corresponding small-scale images $G_s(\mathbf{z}, \mathbf{c})$ and large-scale $G_t(\mathbf{z}, \mathbf{c})$. Then we calculate the cosine similarity $s_{(i,j)}$ between any pair of images in $G_s(\mathbf{z}, \mathbf{c})$ as

$$\mathbf{S}_s(\mathbf{z}, \mathbf{c}) = \{\cos(G_s(z_i, c_i), G_s(z_j, c_j))_{\forall i \neq j}\} \quad (1)$$

and similarly for G_t we have:

$$\mathbf{S}_t(\mathbf{z}, \mathbf{c}) = \{\cos(G_t(z_i, c_i), G_t(z_j, c_j))_{\forall i \neq j}\} \quad (2)$$

Here the \cos denotes the cosine similarity. Next, we normalize these two vectors using softmax and calculate the KL divergence between vectors:

$$\mathcal{L}_{\text{CDC}} = D_{\text{KL}}(\text{Softmax}(\mathbf{S}_s), \text{Softmax}(\mathbf{S}_t)) \quad (3)$$

In this way, one can encourage the G_t to generate samples with a diversity similar to G_s , relieving the mode collapse problem.

Other Techniques: A patchy-level discriminator is also adopted in this work. We divided the astrophysical parameter space into two parts: the anchor region and the rest. The anchor region is a spherical region around training set parameters with a small radius. In this region, the GAN image $G_t(\mathbf{z}, \mathbf{c}_{\text{anch}})$ has a good training sample to compare with. Thus, we apply the full discriminator with these parameters. If \mathbf{c} is located outside the anchor region, we only apply a patch discriminator: in this case, the discriminator does not calculate the loss of the whole image but calculates the loss of different patches of the image.

Since the small-scale information in both training sets is identical, we freeze the first two layers of the discriminator (Mo et al., 2020). We add the small-scale discriminator D_s loss to ensure the correctness of small-scale information. Our code is public-available in this GitHub repo¹.

3. Dataset

The training dataset for this project consists of two parts: a small-scale dataset and a large-scale dataset. All the data are generated with 21cmFAST (Mesinger et al., 2011; Murray et al., 2020), and each simulation has distinct reionization parameters. Our parameters are the ionizing efficiency ζ and the minimum virial temperature T_{vir} . We explored a range of $10 < \zeta < 250$ and $4 < \log T_{\text{vir}} < 6$, and the parameters are sampled with Latin-Hypercube Sampling (McKay et al., 2000).

The small-scale dataset has a resolution of $(64, 64, 512)$ and consists of 30,000 simulations with a comoving box length

¹<https://github.com/dkn16/multi-fidel-gan-21cm>

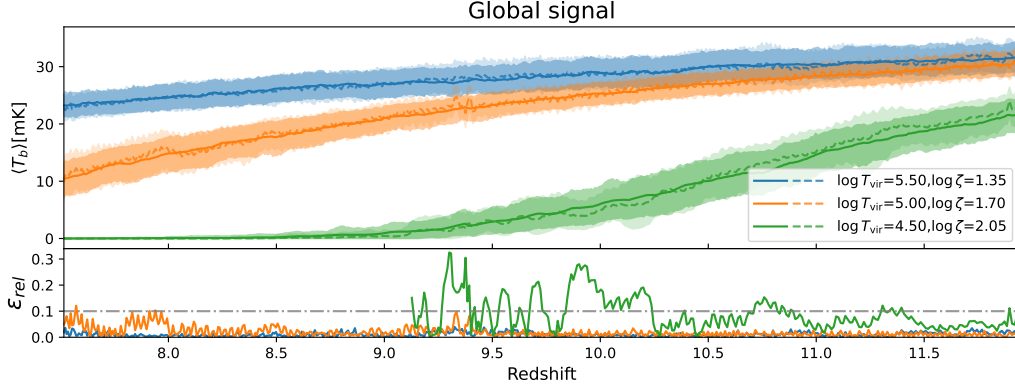


Figure 2. *The upper panel:* global signal reproduced with large-scale GAN. Different colors denote different parameters, the solid line is calculated with the test set, while the dashed line is the GAN result. The shallow shaded region is the 2σ scatter of the GAN images, while the thick shaded region is the 2σ scatter of the test set images. *The lower panel:* relative error between GAN global signal and test set global signal, the grey dot-dashed line represents the 10% error line, while the data points near 0 are neglected.

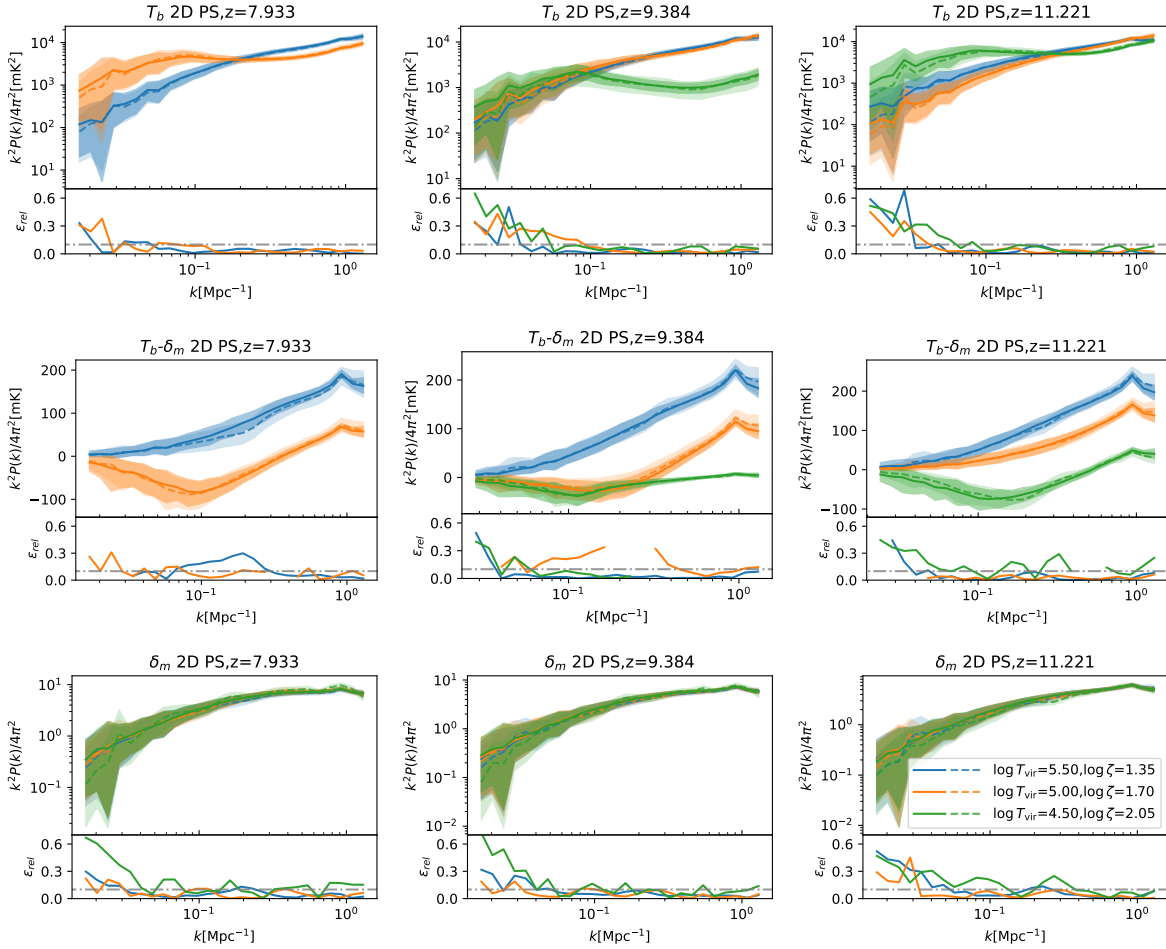


Figure 3. *The upper panel:* the 2D power spectrum of GAN results versus test set PS, each calculated with clips of size (2,256,128). The redshift denotes the redshift of the center slice. Legends are the same as Fig. 2. *The lower panel:* the relative error, same as Fig. 2 but for power spectrum here.

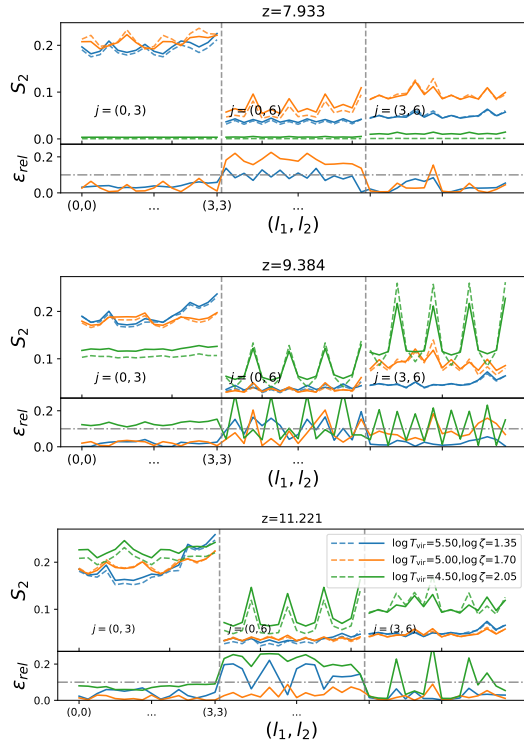


Figure 4. *The upper panel:* the second order scattering coefficients of GAN results versus test set result, each calculated with clips of size (2,256,128). The redshift denotes the redshift of the center slice. Legends are the same as Fig. 2. *The lower panel:* relative error, same as Fig. 2 but for second order scattering coefficients here.

of (128, 128, 1024)Mpc. The third axis (z -axis) is along the line of sight (LoS), spanning a redshift range of $7.51 < z < 11.93$. For each redshift, we run a realization and select the corresponding slice for our final data. We include the matter overdensity field δ_m and the 21 cm brightness temperature T_b field for training. Since the overdensity field is highly correlated with other intensity mappings (IM) like CO and C[II] lines, we expect our method can be transferred to other IM images smoothly. For each sample, we cut four image slices, resulting in 120000 lightcone images with a size of (2, 64, 512) in our small-scale dataset, containing both the overdensity and brightness temperature field.

The large-scale dataset has a (256, 256, 512) resolution and consists of 80 simulations with a comoving box length of (512, 512, 1024)Mpc, covering the same redshift range. As before, for each sample, we cut four slices and obtained 320 lightcone images with a size of (2, 256, 512) in our large-scale dataset.

4. Results

Here we present the evaluation of our model results. A visual inspection of generated samples is shown in Fig. 1. We tested our result on 3 combinations of parameters, each having distinct evolution history. For each parameter combination, we run 4 simulations with distinct initial conditions generated with different random seeds for testing.

Global Signal: We calculated the global 21 cm signal of the GAN results. Limited by the size of the test set, the mean value is calculated with 1024 image samples. Our result is shown in Fig. 2. We see that GAN works well, with an error of mostly less than 5% and a well-matched 2σ region.

Power spectrum (PS): Fig. 3 shows the T_b auto-PS, $T_b - \delta_m$ cross-PS and δ_m auto-PS. GAN results perform well on small scales, with an error of less than 10%, except when the PS is close to 0. On extremely large scales, the error can exceed 50%. This is unsurprising because we lack training samples. The GAN still captures the large-scale power when the T_b signal has a high amplitude. Moreover, the relative error is insignificant compared with the sampling variance.

From T_b auto-PS figures (Fig. 3, top row), the change of lines shows an evolution with the time that power is transferred from small scale to large scale. Again, the accuracy of the cross-PS (Fig. 3, middle row) guarantees the correlation between T_b and δ_m . At early stages, the HI traces the matter field well, and the GAN T_b and δ_m fields have positive cross-correlation at all scales. Later, the cross-correlation becomes negative due to the fact that dense regions hosted ionizing sources earlier and ionized first. Our GAN performs well in reproducing these features. The GAN samples with different parameters have similar matter PS (Fig. 3, bottom row), which agrees with the truth.

Non-Gaussianity: Here we employ the scattering transform (ST, e.g. Mallat, 2012; Allys et al., 2019; Cheng et al., 2020; Greig et al., 2022) coefficients as a non-Gaussian statistic to evaluate our GAN. A detailed description can be found in e.g. Cheng & Ménard (2021). We calculated the second-order ST coefficients S_2 as measures for non-Gaussianity with KYMATIO (Andreux et al., 2020). As the image sample size grows, we set the kernel size scale $j = 0, 3, 6$ to capture more large-scale information. Results are shown in Fig. 4. When $(j_1, j_2) = (0, 3)$, the error is less significant as $\lesssim 10\%$. When $j_2 = 6$ the error exceeds 20%.

5. Summary

In this paper, we introduce the few-shot transfer learning technique to build an emulator for large-scale 21 cm simulations. The large-scale GAN is trained with 80 simulations, and the relative error of statistics is less than 10% on small scales. On large scales, a mild increase in error arises due

to insufficient training samples.

Generating our multi-fidelity dataset requires $\sim 1.2 \times 10^5$ CPU hours, while a purely large scale dataset requires $\sim 1.5 \times 10^5$ CPU hours, with 5000 simulations, an optimistic estimate of dataset size consistent with e.g. Hassan et al. (2022); Andrianomena et al. (2022). Our method reduces the computational cost by 90%, which will enable us to emulate more complex simulations in the future.

Acknowledgements

This work is supported by the National SKA Program of China (grant No. 2020SKA0110401), NSFC (grant No. 11821303), and the National Key R&D Program of China (grant No. 2018YFA0404502). We thank Xiaosheng Zhao, Ce Sui, and especially Richard Grumitt for inspiring discussions. We acknowledge the Tsinghua Astrophysics High-Performance Computing platform at Tsinghua University for providing computational and data storage resources that have contributed to the research results reported within this paper.

References

- Allys, E., Levrier, F., Zhang, S., Colling, C., Regaldo-Saint Blancard, B., Boulanger, F., Hennebelle, P., and Mallat, S. The RWST, a comprehensive statistical description of the non-Gaussian structures in the ISM. *A&A*, 629:A115, September 2019. doi: 10.1051/0004-6361/201834975.
- Alsing, J., Charnock, T., Feeney, S., and Wandelt, B. Fast likelihood-free cosmology with neural density estimators and active learning. *Monthly Notices of the Royal Astronomical Society*, jul 2019. doi: 10.1093/mnras/stz1960. URL <https://doi.org/10.1093%2Fmnras%2Fstz1960>.
- Andreux, M., Angles, T., Exarchakis, G., Leonarduzzi, R., Rochette, G., Thiry, L., Zarka, J., Mallat, S., Andén, J., Belilovsky, E., Bruna, J., Lostanlen, V., Chaudhary, M., Hirn, M. J., Oyallon, E., Zhang, S., Cella, C., and Eickenberg, M. Kymatio: Scattering transforms in python. *Journal of Machine Learning Research*, 21(60):1–6, 2020. URL <http://jmlr.org/papers/v21/19-047.html>.
- Andrianomena, S., Villaescusa-Navarro, F., and Hassan, S. Emulating cosmological multifields with generative adversarial networks. *arXiv e-prints*, art. arXiv:2211.05000, November 2022.
- Cheng, S. and Ménard, B. How to quantify fields or textures? A guide to the scattering transform. *arXiv e-prints*, art. arXiv:2112.01288, November 2021.
- Cheng, S., Ting, Y.-S., Ménard, B., and Bruna, J. A new approach to observational cosmology using the scattering transform. *Monthly Notices of the Royal Astronomical Society*, 499(4):5902–5914, oct 2020. doi: 10.1093/mnras/staa3165. URL <https://doi.org/10.1093%2Fmnras%2Fstaa3165>.
- Goodfellow, I. J., Pouget-Abadie, J., Mirza, M., Xu, B., Warde-Farley, D., Ozair, S., Courville, A., and Bengio, Y. Generative Adversarial Networks. *arXiv e-prints*, art. arXiv:1406.2661, June 2014.
- Greig, B. and Mesinger, A. Simultaneously constraining the astrophysics of reionisation and the epoch of heating with 21cmmc. *Proceedings of the International Astronomical Union*, 12(S333):18–21, oct 2017. doi: 10.1017/s1743921317011103. URL <https://doi.org/10.1017%2Fs1743921317011103>.
- Greig, B., Ting, Y.-S., and Kaurov, A. A. Detecting the non-Gaussianity of the 21-cm signal during reionisation with the Wavelet Scattering Transform. *arXiv e-prints*, art. arXiv:2207.09082, July 2022.
- Hassan, S., Villaescusa-Navarro, F., Wandelt, B., Spergel, D. N., Anglé s-Alcázar, D., Genel, S., Cranmer, M., Bryan, G. L., Davé, R., Somerville, R. S., Eickenberg, M., Narayanan, D., Ho, S., and Andrianomena, S. HI-Flow: Generating diverse hi maps and inferring cosmology while marginalizing over astrophysics using normalizing flows. *The Astrophysical Journal*, 937(2):83, sep 2022. doi: 10.3847/1538-4357/ac8b09. URL <https://doi.org/10.3847%2F1538-4357%2Fac8b09>.
- He, K., Zhang, X., Ren, S., and Sun, J. Deep residual learning for image recognition, 2015. URL <https://arxiv.org/abs/1512.03385>.
- Ho, M.-F., Bird, S., and Shelton, C. R. Multifidelity emulation for the matter power spectrum using gaussian processes. *Monthly Notices of the Royal Astronomical Society*, 509(2):2551–2565, oct 2021. doi: 10.1093/mnras/stab3114. URL <https://doi.org/10.1093%2Fmnras%2Fstab3114>.
- Kannan, R., Garaldi, E., Smith, A., Pakmor, R., Springel, V., Vogelsberger, M., and Hernquist, L. Introducing the THESAN project: radiation-magnetohydrodynamic simulations of the epoch of reionization. *Monthly Notices of the Royal Astronomical Society*, 511(3):4005–4030, dec 2021. doi: 10.1093/mnras/stab3710. URL <https://doi.org/10.1093%2Fmnras%2Fstab3710>.
- Karras, T., Aila, T., Laine, S., and Lehtinen, J. Progressive Growing of GANs for Improved Quality, Stability, and Variation. *arXiv e-prints*, art. arXiv:1710.10196, October 2017. doi: 10.48550/arXiv.1710.10196.

- Karras, T., Laine, S., Aittala, M., Hellsten, J., Lehtinen, J., and Aila, T. Analyzing and improving the image quality of StyleGAN. In *Proc. CVPR*, 2020.
- Kennedy, M. and O’Hagan, A. Predicting the output from a complex computer code when fast approximations are available. *Biometrika*, 87(1):1–13, 03 2000. ISSN 0006-3444. doi: 10.1093/biomet/87.1.1. URL <https://doi.org/10.1093/biomet/87.1.1>.
- List, F. and Lewis, G. F. A unified framework for 21 cm tomography sample generation and parameter inference with progressively growing GANs. *Monthly Notices of the Royal Astronomical Society*, 493(4):5913–5927, April 2020. doi: 10.1093/mnras/staa523.
- Liu, B., Zhu, Y., Song, K., and Elgammal, A. Towards Faster and Stabilized GAN Training for High-fidelity Few-shot Image Synthesis. *arXiv e-prints*, art. arXiv:2101.04775, January 2021. doi: 10.48550/arXiv.2101.04775.
- Mallat, S. Group invariant scattering. *Communications on Pure and Applied Mathematics*, 65(10): 1331–1398, 2012. doi: <https://doi.org/10.1002/cpa.21413>. URL <https://onlinelibrary.wiley.com/doi/abs/10.1002/cpa.21413>.
- McKay, M. D., Beckman, R. J., and Conover, W. J. A comparison of three methods for selecting values of input variables in the analysis of output from a computer code. *Technometrics*, 42(1):55–61, 2000.
- Mesinger, A., Furlanetto, S., and Cen, R. 21cmfast: a fast, seminumerical simulation of the high-redshift 21-cm signal. *Monthly Notices of the Royal Astronomical Society*, 411(2):955–972, 02 2011. ISSN 0035-8711. doi: 10.1111/j.1365-2966.2010.17731.x. URL <https://doi.org/10.1111/j.1365-2966.2010.17731.x>.
- Mo, S., Cho, M., and Shin, J. Freeze the discriminator: a simple baseline for fine-tuning gans, 2020. URL <https://arxiv.org/abs/2002.10964>.
- Murray, S. G., Greig, B., Mesinger, A., Muñoz, J. B., Qin, Y., Park, J., and Watkinson, C. A. 21cmfast v3: A python-integrated c code for generating 3d realizations of the cosmic 21cm signal. *Journal of Open Source Software*, 5(54):2582, 2020. doi: 10.21105/joss.02582. URL <https://doi.org/10.21105/joss.02582>.
- Ojha, U., Li, Y., Lu, J., Efros, A. A., Lee, Y. J., Shechtman, E., and Zhang, R. Few-shot Image Generation via Cross-domain Correspondence. *arXiv e-prints*, art. arXiv:2104.06820, April 2021.
- Tröster, T., Ferguson, C., Harnois-Déraps, J., and McCarthy, I. G. Painting with baryons: augmenting N-body simulations with gas using deep generative models. *MNRAS*, 487(1):L24–L29, July 2019. doi: 10.1093/mnrasl/slz075.
- Yiu, T. W. H., Fluri, J., and Kacprzak, T. A tomographic spherical mass map emulator of the KiDS-1000 survey using conditional generative adversarial networks. *JCAP*, 2022(12):013, December 2022. doi: 10.1088/1475-7516/2022/12/013.
- Zhao, X., Mao, Y., and Wandelt, B. D. Implicit likelihood inference of reionization parameters from the 21 cm power spectrum. *The Astrophysical Journal*, 933(2):236, jul 2022. doi: 10.3847/1538-4357/ac778e. URL <https://doi.org/10.3847/1538-4357/ac778e>.

A. Comparison with previous work

Several noteworthy applications of GAN in astronomy have been extensively explored in previous studies (e.g., List & Lewis, 2020; Andrianomena et al., 2022; Yiu et al., 2022; Tröster et al., 2019). Previous works have made significant progress in utilizing innovative GAN structures such as the progressively growing GAN (PGGAN) (Karras et al., 2017) and stabilized GAN (Liu et al., 2021). These studies have demonstrated sub-percent-level accuracy, as assessed by various statistical measures, for unconditional emulation, and achieved accuracy at the ten percent level for conditional emulation. A comparison between our results and previous findings is presented in Table 1. By employing the StyleGAN2 architecture, we have achieved percent-level accuracy in conditional emulation with sufficient training samples, as validated by various statistical measures. In the few-shot learning scenario, our GAN exhibits similar accuracy on a small scale and demonstrates a moderate increase on a larger scale. Furthermore, our large-scale GAN, combined with few-shot transfer learning techniques, allows for computational resource savings ranging from 90% to 99%, depending on different estimations.

B. Test on mode collapse

B.1. Visual inspection

To assess the diversity of our model, we conducted a visual inspection. We generated multiple realizations for both GAN samples and simulation samples, as illustrated in Fig. 5. Upon careful observation, we observed that the shape and size of ionized bubbles exhibit variation across different GAN samples, indicating the absence of any specific preference for bubble features. Furthermore, the locations of ionized bubbles also appear random, as no discernible trend or pattern was observed among the samples we examined.

B.2. Pixel level variance

In addition to visual inspections, we also computed the standard deviation of the T_b field for each pixel, as depicted in Fig. 6. Our aim was to observe any potential decrease in the standard deviation, which could indicate mode collapse. Upon analyzing the results in Fig. 6, we noticed that the variance for both GAN and simulation samples appeared similar, particularly for higher T_b values. However, we observed mild fluctuations in the standard deviation when the T_b value was low. Based on this analysis, we can conclude that there is no clear evidence of significant mode collapse at the pixel level.

B.3. Feature level variance

Lastly, we computed the 2σ scatter of the second-order ST coefficients (S_2) for the T_b field, which serves as a representation of image features. The results are presented in Figures 7-9. Consistent with the analysis in Section 4, we selected the scales (j_1, j_2) as (0,3), (0,6), and (3,6) to capture both small and large-scale features.

Upon examination, we observed that in most cases, the 2σ scatter of GAN features overlapped with that of simulation samples, indicating the absence of mode collapse at the feature level. However, in the bottom subplot of Fig. 8, we noticed a deviation in both the mean value and 2σ scatter for certain features at the super-large scale. This suggests a slight mode collapse issue in the generated images at that particular scale.

In conclusion, our analysis indicates that there is no strong evidence of mode collapse at the feature level. The GAN samples generally mimic the behavior of the simulation samples quite well, except when the T_b approaches zero.

Table 1. A comparison of accuracy and cost of various methods. Large-scale GAN is training GAN with only large-scale image samples, and the performance is estimated. The cost here is the CPU hours used to generate the dataset.

Method	Relative Error		Cosmic Variance	Cost [CPU hours]
	At small scales	At large scales		
Small-scale GAN	$< 10\%$	—	Large	1×10^4
Large-scale GAN (estimated ^a)	$< 10\%$	$< 10\%$	Small	$(1.5 - 9) \times 10^5$
Few-shot GAN (this work)	$< 10\%$	20% – 50%	Small	1.2×10^4

^aAccording to related work, 5000 large-scale simulations is an optimistic estimation for the necessary training samples (e.g. Hassan et al., 2022; Andrianomena et al., 2022), which will take 1.5×10^5 CPU hours; to ensure the 10% accuracy and to make a fair comparison, 30000 simulations are required, which will cost 9×10^5 CPU hours.

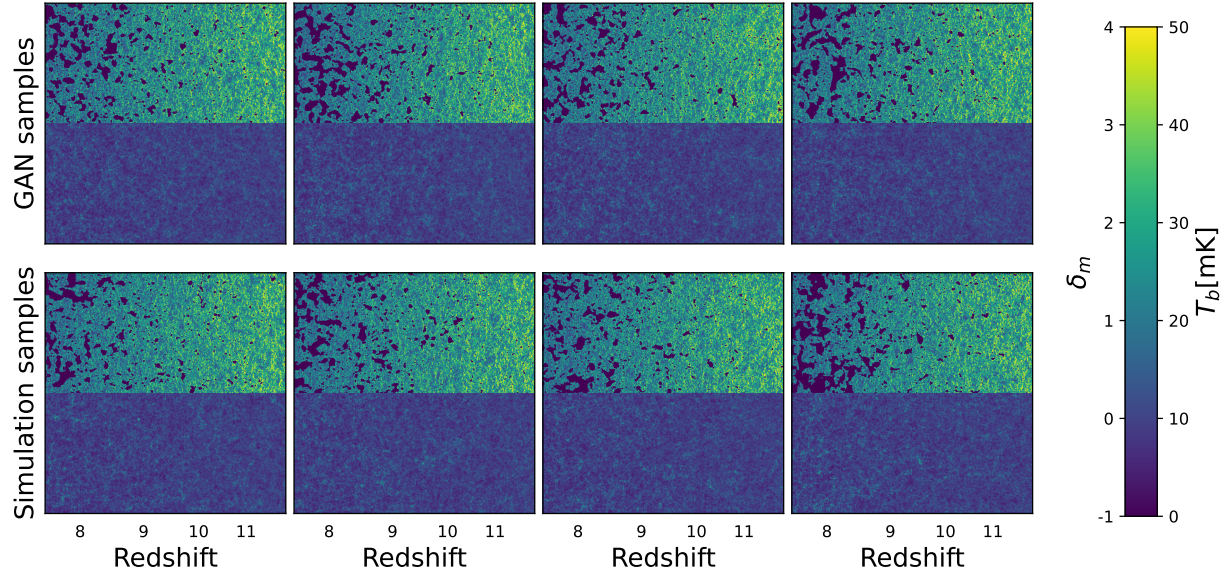


Figure 5. Here we present four distinct realizations for both GAN and simulation samples, allowing for visual inspection. These realizations were generated with the parameters $\log T_{\text{vir}} = 5.50$ and $\log \zeta = 1.70$. The upper panel displays the GAN samples, while the lower panel showcases the simulation samples. Each realization was computed using a unique latent vector (for GAN) or initial condition (for simulation). Within each subplot, the upper half represents the brightness temperature field, while the lower half represents the overdensity field.

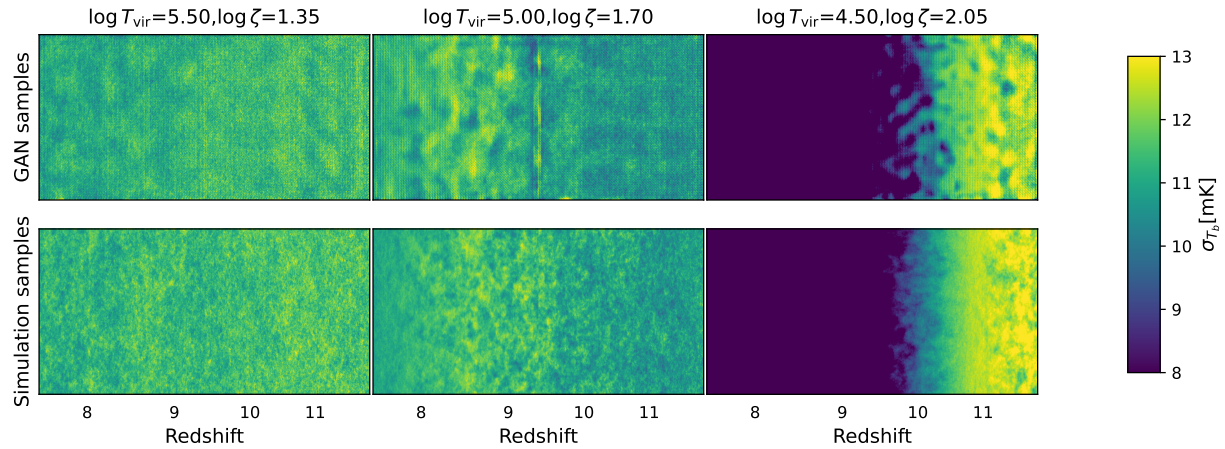


Figure 6. The standard deviation in each pixel is calculated for the 21 cm T_b map. The upper panel is for the GAN samples while the lower panel is for the simulation samples.

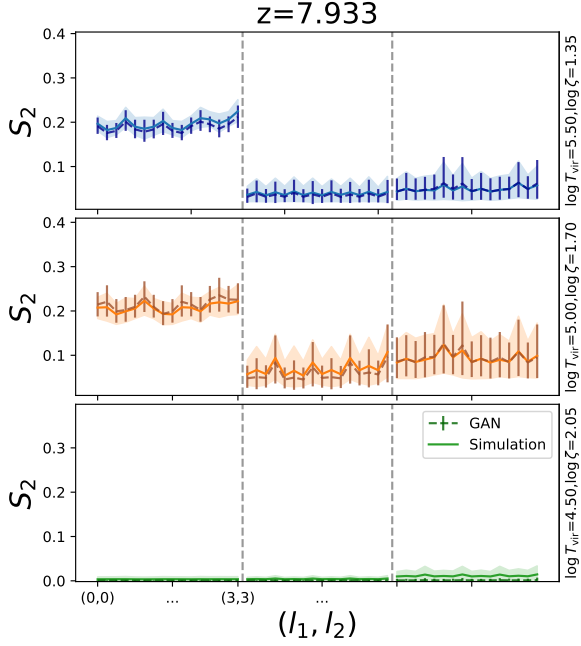


Figure 7. The 2σ scatter of S_2 for in simulations and GAN samples at $z = 7.933$. The solid line is for the simulation mean value, while the dashed line is for GAN mean. Shaded region is the 2σ scatter for simulation samples while the error bar is for GAN samples. Different plot corresponds to different reionization parameters, as is shown on the right of each plot.

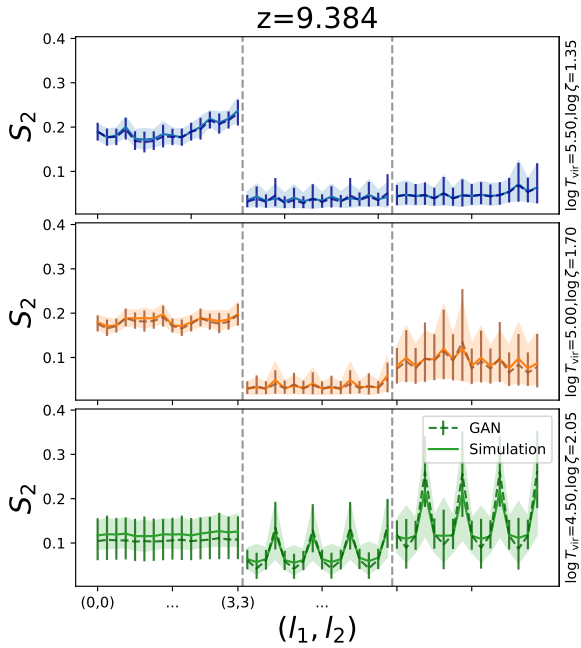


Figure 8. Same as Fig. 7, but for $z = 9.384$.

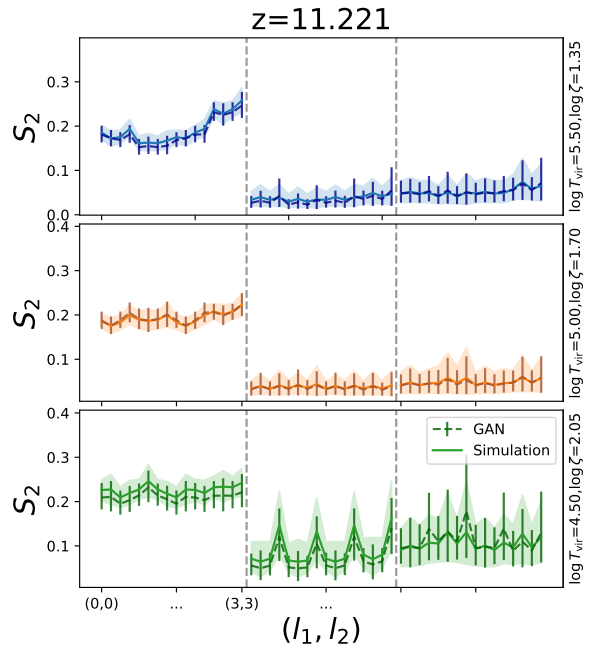


Figure 9. Same as Fig. 7, but for $z = 11.221$.